High resolution imaging of flameless and distributed turbulent combustion

C. Duwig [a,c], B. Li [b], Z.S. Li [b,*], M. Aldén [b]

[a] Haldor Topsoe A/S, R&D Division, DK-2800 Lyngby, Denmark
[b] Division of Combustion Physics, Lund University, P.O. Box 118, S-22100 Lund, Sweden
[c] Division of Fluid Mechanics, Lund University, S-22100 Lund, Sweden

ABSTRACT

Planar laser-induced fluorescence (PLIF) and Rayleigh scattering measurements were used for the study of turbulence/combustion interactions in distributed reaction regimes including flameless or MILD combustion. A novel laboratory scale burner (Distributed and Flameless Combustion Burner – DFCB) was used to reach uniquely high Karlovitz numbers, presently reported up to 14,400. It consists of a highly turbulent piloted high speed jet burner with a vitiated coflow. Six cases are reported whereas two of them (leaner cases) led to an invisible reacting zone, though still emitting light in the UV and near infrared range. Simultaneous OH/CH$_2$O PLIF image with 50 μm spatial resolution were achieved to capture the variation of intermediate species in the reaction layer. When complemented with temperature images obtained by Rayleigh scattering measurement, it provided insights of the reaction front structures as well as measures of the flame brush thicknesses. In particular, variations in the jet velocity highlighted the influence of turbulent mixing (hence turbulence/chemistry interaction) on the flame structures as depicted by the formation of relatively large pools of CH$_2$O. Further, variations in the jet stoichiometry impacted on the reaction zone visibility but only marginally on the intensity and moderately on the overall shape of the OH and CH$_2$O signals.

© 2011 The Combustion Institute. Published by Elsevier Inc. All rights reserved.

1. Introduction

Despite more than 60 years of research, turbulent combustion still poses considerable challenges for the community [1]. The interaction between turbulent structures and chemical reactions features a multi-scale non-linear problem. In the limit of a very/infinitely thin reaction layer, the flamelet concept has been successful [2]. For example, typical low Reynolds number (Re) laboratory scale experiments often fall in the flamelet regime and have led to numerous studies and successful modelling activities [1]. However, this regime is not always relevant to industrial combustion devices which commonly operate at very high Re in the distributed combustion regime (high Karlovitz number – Ka).

A modern solution to avoid NO$_x$/soot formation and unwanted peak temperature consists of diluting the reactants with large amount of inert gases [3–5]. Practically, this can be done by using low calorific value fuels, dilution by massive injection of steam or intensive exhaust gas recirculation (EGR). As a consequence, the reaction rate is considerably lowered by the dilution and the reaction zone expands over a significant fraction of the combustor volume. It departs significantly from the flamelet regime. This technique is frequently referred as MILD (Moderate or Intense Low oxygen Dilution). Similarly, one may consider very lean or diluted flames (with significant preheat) which are almost sightless referring to flameless combustion. In all cases, one shall find the right balance between reactant dilution and preheating to maintain complete combustion. A common solution is to ensure that the fresh reactants entrain a large amount of flue gases with a mixing time scale much shorter than the corresponding chemical time scale. In other words, the intention is to mix fast enough so that no chemical reactions have time to take place before a given level of dilution is achieved. To maintain an operating temperature suitable for combustion, regenerators are often used to introduce heat-exchange between the flue gas and the incoming combustion air. As a result, the energy efficiency of the furnace may increase by about 50% [6,7] while keeping the harmful emission very low.

At present, engineering examples of both furnaces [3–9] and model gas turbine combustors [10,11] operating in flameless mode are available in the literature. The technology is relatively well established for furnace applications, but it is not mature for gas turbine combustors yet. The main difference lies in the available space for adding additional devices, the operating conditions as well as the possibility of heat-removal. For example, regenerators can not be used in gas turbines and aero-engines and the dilution/preheating is to be done by aerodynamic means only [10]. Furthermore, gas turbine and aero-engines would operate lean adiabatic (high oxygen content) combustion while furnaces feature

higher equivalence ratio (low oxygen content) and heat-removal. Pioneering works including high speed jet combustors [10,11] and stagnation point reverse flow combustor [12] have shown promising results for adapting flameless technology to gas turbine applications. However, these activities are limited by the lack of theoretical understanding for the driving mechanism of flameless combustion [4,7]. High Ka combustion in general is not well understood and has not been investigated extensively. The reason lies in the difficulties of reaching this regime in low Re laboratory scale experiments [1]. The newly designed burners and recent studies have opened new avenues, as will be exemplified in the following.

Very recent studies have been concentrated on laboratory scale experiments focusing on distributed [13–15] and MILD [16–18] combustion taking advantage of laser diagnostics. These burners often consist of a central moderate or high speed jet (fuel or fuel air mixture) surrounded by a heated coflow. Flexibility in the composition of the jet and coflow gives access to a wide range of combustion regime. For example, Dally et al. [17] showed changes in the reacting layer structure when varying the oxygen content of the coflow (from distributed flame to MILD). Furthermore, Gordon et al. [14] reported that a methane lifted flame is preceded by pools of formaldehyde acting as 'precursor' for auto-ignition which seems to occur as well in the MILD combustion regime [18]. In addition, temperature imaging with high resolution enables the temperature gradient to be captured and the thickening of the reaction front to be quantified. There is a valuable insight when combining advanced laser diagnostic techniques for capturing the details of the turbulence chemistry interaction in distributed and flameless combustion regimes.

The present work focuses on that direction and contributes with a novel burner enabling operation at a uniquely high Ka (described in the next section). Further we present the laser diagnostic system for acquiring images with high spatial resolution and to precisely capture the reacting zones. The result section starts with snapshot images for evidencing turbulence/chemistry interaction. It is supplemented by statistical data for quantifying the effects of stoichiometry (hence Ka) variations upon the combustion.

2. Distributed and Flameless Combustion Burner

A novel burner for emulating very high Ka combustion is presented in this paper and referred as Distributed and Flameless Combustion Burner (DFCB). The burner is located at the Division of Combustion Physics at Lund University and operates at atmospheric pressure without confinement. As presented in Fig. 1, it consists of a central metallic plug (diameter 0.01 m) with a 0.0015 m diameter hole in the centre surrounded by a McKenna burner. The central hole

discharges a jet consisting of a fresh methane/air mixture at variable fuel/air equivalence ratio Φ_j. The methane/air mixing is considered to be perfectly mixed with mixing initiated far upstream of the burner.

The surrounding McKenna burner stabilises a laminar planar flame covering an annulus of inner and outer radius being 0.01 m and 0.06 m, respectively. This laminar flame is fed by a methane/air mixture at equivalence ratio 0.75 which is kept constant for all cases reported presently. The laminar flame is located 0.002 m below the jet nozzle. Assuming a freely propagating laminar flame, the corresponding thermal flame thickness was estimated (using Cantera [19] and GRI3.0 [20]) to be about 0.0006 m leaving sufficient space for reaching a burnt state. It results in a constant steady coflow consisting of burnt gases (composition in mol%: H_2O 14.5; CO_2 7.3; O_2 4.7; rest is N_2) at 1920 K. Alternatively, one may model the McKenna burner flame by a burner stabilized flame which would give a lower burnt gas temperature (1807 K) without changing the burnt gas composition. The temperature measurements presented later estimate the actual coflow temperature at 1850 K. The coflow velocity is kept at 0.15 m/s prior to the laminar flame resulting in 0.96 m/s after thermal expansion (using 1920 K as unburnt temperature). As seen on the temperature images, the coflow is sufficiently large to shield the jet, avoid interactions between the jet and the surrounding air and ensure constant coflow temperature, at least in the region of interest.

Inside the plug, the fresh gas mixture flows through a cylinder of diameter 0.008 m ending by a sudden contraction to restrict the jet diameter to $d = 0.0015$ m. A four-branches cross obstacle (star) positioned 0.02 m upstream of the contraction perturbs the laminar flow. A large eddy simulation of the plug internal flow (not presented here) indicates that the obstacle induces a quasi-periodic forcing on the jet (Strouhal number based on the jet bulk velocity U_{JET}: $St = fd/U_{JET} \sim 0.02$) of amplitude $\sim$10%. The forcing was designed to trigger the azimuthal inhomogeneity of the flow, hence promote stream-wise vortex tubes and enhance the hot gas entrainment (e.g. [21]). The copper brass plug is water cooled avoiding any significant preheating of the jet before issuing in the coflow. This was verified by Rayleigh thermometry, giving a temperature of 320 K along the centreline $5d$ downstream of the expansion.

As compared to the works cited in the introduction, the present burner features a smaller jet but operates at similar or higher bulk velocities. The higher velocities together with the contraction to a smaller jet diameter ensure a higher strain rate downstream of the nozzle and a smaller Kolmogorov length scale (turbulent case only) than previous studies. We may estimate a global Ka following Dunn et al. [22] as:
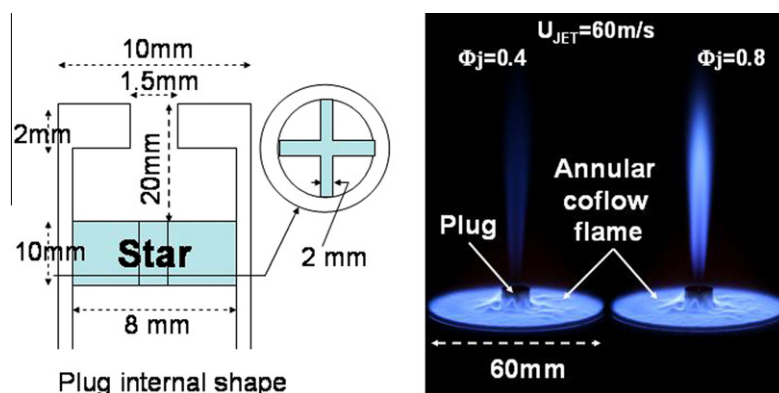

Fig. 1. Schematic of the plug and burner layout with examples of premixed jet combustion featuring strong and weak light emissions (respectively Φ_j = 0.8 and 0.4, exposure time 1 s).

$$Ka \sim \frac{1}{\sqrt{15}}\frac{t_c}{t_K} \sim \frac{1}{\sqrt{15}}\frac{\frac{\delta_L}{S_L}}{\left(\frac{Lv}{u'^3}\right)^{0.5}} \sim \frac{\delta_L (I \cdot U_{JET})^{1.5}}{S_L\sqrt{15dv}} \qquad (1)$$

where u', L, v, S_L, δ_L and I are the velocity fluctuation, the turbulent integral length scale, the kinematic viscosity (here taken equal to 1.6×10^{-5} m^2/s), the laminar flame speed, the laminar flame thickness and the turbulence intensity, respectively. We note that Eq. (1) was derived assuming isotropic turbulence and that the fluctuation is modelled as a fraction of the jet bulk velocity. It provides therefore only an estimate of the global Ka, giving an idea of the order of magnitude rather than an exact value. The laminar flame properties were computed using Cantera [19] together with the GRI3.0 [20] and I was taken to be 0.1, which is inline with the measurements of Dunn et al. [22]. Considering a jet speed U_{JET} = 100 m/s, we obtain Ka ~ 60 for $\Phi_j = 1$ and up to Ka $\sim 31{,}000$ for $\Phi_j = 0.4$, although with the jet Reynolds number is kept moderate at Re ~ 9300. These figures indicate that the DFCB enables the browse from thickened flame regime to distributed reaction regime and flameless combustion regime as well as reaching uniquely high Ka for laboratory scale experiments.

We consider presently six cases with $\Phi_j = 0.4$, 0.8 and 6.0 as summarized in Table 1. The jet bulk velocity is also varied considering U_{JET} = 30 (laminar unsteady reacting jet) and 60 m/s (turbulent reacting jet). The fuel rich jet features typical MILD conditions [15–17], i.e. combustion in hot oxygen-depleted gas (although the temperature is presently higher than in [15–17]). At $\Phi_j = 0.8$, we reach a thickened or distributed premixed flame similar to those reported in [22]. The very lean jet is similar to the conditions observed in model gas-turbine combustors [10,11] with a large excess of oxygen. Unlike [10,11], we do not preheat the fresh air/fuel mixture. Instead we are compensating with a higher coflow temperature. The coflow temperature was chosen to balance the cold methane/air mixture so that a non-reacting mixture of 50% fresh/50% vitiated gas will reach about 1100 K and mimic the conditions reported in [10]. Of course, the thermo-chemistry of the two combustion systems differs. In particular the most reactive mixture fraction is changed when changing the preheat temperature but it was not possible to proceed differently with the present setup.

In order to appreciate the effect of strain and turbulence upon the reacting layer, a reference laminar flame is computed for each stoichiometry. It consists of a laminar counter flow opposing a stream of fresh methane/air mixture (at $\Phi_j = 0.4$, 0.8 or 6.0) to a stream of vitiated gas, identical to the coflow gas. The strain is kept constant to 220 s^{-1}. The counter-flow configuration was chosen presently as freely propagating flame would not exist for the leanest or richest cases. In addition, other strain rates were tested without significant effect on Ka. We note that in the counter-flow configuration, the reaction is secured thanks to the hot coflow and reactions were found to occur at temperatures above 1100 K which falls in the domain of validity of GRI3.0. Table 2 summarises the characteristic thicknesses based on the steepest OH and temperature gradients. As it will be detailed later, a spatial resolution (SR) of ~ 50 μm has been achieved in the present PLIF (planar

Table 1
Flame operating conditions. The Karlovitz numbers are estimated as in [15] and are only given for the turbulent cases, except at rich jet conditions where the flame speed can not be defined.

U_{JET} = 30 m/s			U_{JET} = 60 m/s		
Φ_j	Ka	Re	Φ_j	Ka	Re
0.4	–	2810	0.4	14,400	5620
0.8	–	2810	0.8	50	5620
6.0	–	2810	6.0	–	5620

Table 2
Counterflow laminar flame characteristic thicknesses at different equivalence ratios based on the steepest OH (δ_{OH}) and temperature (δ_T) gradient. Strain rate is kept constant to ~ 220 s^{-1} for all cases.

Φ_j	δ_{OH} (m)	δ_T (m)	Max($|\nabla T|$) (K/m)
0.4	0.00042	0.00150	1.10×10^6
0.8	0.00023	0.00053	3.15×10^6
6.0	0.00068	0.00205	0.79×10^6

laser-induced fluorescence) measurements. For the very lean and rich cases, the laminar thermal layers extend over more than 30 SRs so that the temperature rise will be well resolved in the Rayleigh images. The OH gradients are steeper but can still be captured on at least about 10 SRs, hence are well resolved by the present imaging techniques. The case at $\Phi_j = 0.8$ presents a thinner front and the steepest temperature gradient will be captured over at least ~ 10 SRs while the steepest OH gradient would spread over at least 5 SRs. Although the resolution is lower than in the two other cases, it is still adequate and the smoothing inherent to the imaging technique would not affect the results.

We should also point out that the thermal and OH thicknesses are of the order of the jet diameter indicating that a laminar flame cannot settle undisturbed in the shear-layer of the jet. Instead, the reacting layer is expected to be affected by shear-layer and possibly by a large range of turbulent structures (including energetic large eddies). Therefore the thinner layers are not likely to result from a reaction–diffusion balance but would relate to the characteristic thickness of the device. For a jet, one would consider the shear-layer thickness being a fraction of the nozzle. For the present jet, one estimates the shear-layer to be at most $\sim 1 \times 10^{-4}$ m which is thinner than the laminar flames discussed above. However, even with such a thin shear-layer, the spatial resolution is adequate.

3. Diagnostic techniques

Flame emission spectra under different flame conditions were analyzed with a fibre-coupled compact spectrometer (Ocean Optics, USB2000, grating: 600 grooves/mm blazed at 300 nm) over spectra range of 200–850 nm with a spectral resolution of 1.3 nm. Flame emission was collected by a spherical lens (f = 50 mm, f/1), and 1:1 imaging of the flame was achieved. At the imaging plane a fibre collimator, 0.5 cm in diameter, was placed ensuring a small detecting volume at 3 cm (20 L/D) height above the jet, in this way providing certain spatial resolution. The spectral response of the spectrometer and the related optical system at different wavelength has been calibrated with two calibration lamps, a tungsten halogen lamp (Labsphere, IES 1000) for Vis–NIR region and a deuterium lamp (Cathodeon Ltd., R70) for UV region, to cover the whole spectral range before the flame measurements.

The chosen laser diagnostic system consists of a planar laser-induced fluorescence (PLIF) system for simultaneous CH$_2$O/OH imaging as well as a Rayleigh scattering (RS) system for temperature measurements. The formaldehyde imaging is aimed at capturing the 'precursor' region, while OH marks the 'oxidation' region, see [14,17]. The experimental setup for simultaneous PLIF of OH and CH$_2$O consists of two independent laser and ICCD camera systems enabling simultaneous imaging of the two species. For the excitation of formaldehyde, a Nd:YAG laser (Quantel Brilliant B) was employed to provide the 355 nm laser beam with 130 mJ per pulse in the probed volume. The fluorescence was collected and imaged with an ICCD camera (Princeton PI-MAX, 512 × 512 pixels) and a Nikon objective (f/1.2, 50 mm) through a Schott long-pass filter (GG385). For OH PLIF imaging the $Q_1(8)$ line belonging to the

$X^2\Pi - A^2\Sigma^+$ (0, 1) band at 283.553 nm was excited using the second harmonic radiation from a dye laser (Continuum ND60, Rhodamine 590) pumped by an Nd:YAG laser (Spectra-Physics, PRO-290) providing 12 mJ per pulse UV beam in the laser sheet, and the fluorescence from the $X^2\Pi - A^2\Sigma^+$ (1, 1) and (0, 0) bands at around 308 nm was collected through two combined Schott filters (WG305 and UG11) and a UV objective (UV Nikon, 105 mm focal length), and finally captured by another ICCD (Princeton PI-MAX, 512×512 pixels). For simultaneous measurements of OH and CH$_2$O, the two independent excitation and detection systems were synchronized to each other with a time delay around 50 ns to avoid spectral interferences. A dichroic mirror (HR355) was used to overlap the two laser beams, and they were then formed into overlapping vertical laser sheets of 2 cm height after going through a cylindrical lens (-40 mm focal length) and a spherical lens (200 mm focal length) as well as a slit aperture. The thickness of the laser sheets directly calculated for a Gaussian beam with the parameters of the adopted optics was ~ 15 μm at the focal position. Considering spatial mode structure of the real laser beam and the ~ 2 mm spanning of the imaging area around the beam focus, also based on the measurement by a razor blade, the thickness of the two beams were estimated to be around 50 μm. Besides, the spatial resolution of the optical system on the image plane is given by conventional Modulation Transfer Function (MTF) method. For that purpose, we adopted a resolution target (Newport, USAF-1951, RES-1) consisting of groups of line-space pattern with different spatial frequencies. The image of this target was taken by the same optical system, and the cut-off frequency (of which the contrast of the line-space pattern is equal to zero) was found out. Then as a conservative estimation, we define the frequency one grade below the cut-off frequency on the target as the limitation of this optical system, and the line width of this pattern as the spatial resolution, which is about 50 μm. Thus the OH and formaldehyde PLIF system can provide a spatial resolution of 50 μm $\times$ 50 μm $\times$ 50 μm. The achieved signal-to-noise ratio for single shot OH PLIF is about 16 and for single shot formaldehyde PLIF is about 8.

In the experimental setup for 2-D (two dimensional) Rayleigh thermometry, the second harmonic radiation (532 nm, 400 mJ) from a Nd:YAG laser (Spectra-Physics, PRO-290) was adopted as light source, which was formed into a laser sheet by a cylindrical lens (-40 mm focal length) and a spherical lens (300 mm focal length) as well as a slit aperture. The laser sheet was 2 cm in height and 100 μm in thickness, and was send through the flame 5 mm above the burner surface. An ICCD camera (Princeton PI-MAX, 512×512 pixels) coupled to a Nikon objective (f/2.8, 50 mm) was placed perpendicular to the laser sheet to collect the Rayleigh scattering signal. The resulting images captured a squared region of $13d \times 13d$ while the jet diameter is resolved by ~ 37 pixels, which provides a spatial resolution of 50 μm $\times$ 50 μm $\times$ 100 μm. To evaluate temperature information from the flame Rayleigh scattering intensities, Rayleigh scattering from pure nitrogen flow at room temperature was collected to be used as *in situ* calibration source. Besides, taking into account the composition of the burned gas calculated by GRI3.0 mechanism [20], and the Rayleigh cross-section values for different species [23], we found that the effective Rayleigh cross-section for burned gas and unburned gas is almost the same for the cases of $\Phi < 1$. Then the constant effective Rayleigh cross-section was adopted in evaluating the whole Rayleigh image for turbulent lean cases ($U_{JET} = 60$ m/s, $\Phi_j = 0.4$ and 0.8), which introduces less than 3% error in the temperature field. The temperature fields were further de-noised using a total variation noise removal technique [24] and a low-pass Gaussian filter (width 2 pixels) was applied. The signal to noise ratio was 20 before de-noising and 100 after.

We stress that the present measurements (both PLIF and Rayleigh) have a fine spatial resolution comparing favourably with papers from the literature. In addition, 50–100 μm is sufficient to capture the shear-layer thickness, as discussed earlier. In turbulent cases, one may expect a thickening of the reacting fronts, hence distribution over a larger number of pixels and an improved resolution. Another unique feature of the present setup is the ability to capture on a single image a large portion of the reacting jet, not only some details in a narrow band. It enables the interaction between chemical oxidation and relatively small scale turbulence along the jet shear-layer to be visualized simultaneously.

For each condition, an ensemble of 500 samples was collected and used for the data analysis. Each image corresponds to a (y, r) plane, where y is the coordinate along the jet axis ($y = 0$ chosen at the plug exit) and r is the distance from the axis. The normalized cross-correlation C of the OH and CH$_2$O signals is computed as:

$$C(y,r) = \frac{\langle OH \cdot CH_2O \rangle - \langle OH \rangle \cdot \langle CH_2O \rangle}{\sqrt{\langle OH^2 \rangle - \langle OH \rangle^2} \cdot \sqrt{\langle CH_2O^2 \rangle - \langle CH_2O \rangle^2}} \qquad (2)$$

where $\langle \ \rangle$ denotes the ensemble averaging operation. We should stress that the computation of C based on non-quantitative measurements can be misleading, as OH and CH$_2$O PLIF intensity are not necessarily proportional to the respective concentrations. In the present case, the fluorescence signals were taken with saturated PLIF and differences and only the sign of the C-fields will be presented rather than exact value. So, the qualitative nature of the measurements is not expected to bias the conclusions.

Finally, the normalized gradient denoted G is computed from the 2D temperature field as:

$$G(y,n) = \frac{\max\limits_r(|\nabla T_{2D}|)}{\max(|\nabla T_{lam}|)} \qquad (3)$$

where $\max_r$ denotes the maximum along the radius, here of the norm of the planar temperature gradient (limited to two dimensions). The 2D gradient was computed using a second order centred finite difference scheme. A fourth order scheme was also tested but did not show any significant difference with the second order (maximum discrepancy of 4%). G is a function of the axial coordinate and the sample number n. The gradient is normalized by the norm of the maximum temperature gradient in the counter-flow flame discussed previously. These values are presented in Table 2. The G samples lines for computing the probability density function (PDF) are located on a 21 pixels wide band centred on $y/d = 8$.

4. Results and discussions

4.1. Visual investigations and natural emissions

Flameless combustion firstly drew special attention from its property of non-visibility by human eye. However, detailed spectral properties of emission from these reacting gas plumes are unclear and can in principle provide an insight into the phenomenon. The emission spectra at different flame cases were collected from a spot (3 mm diameter) at $y/d = 20$ down stream above the plug and the results are presented in Fig. 2. For all cases in the collected spectra, emissions between 700 and 850 nm are almost identical and correspond to hot water lines [25], contributing to a barely visible dark red colour. For the very lean case ($\Phi_j = 0.4$), there are almost no visible radiation in the 400–700 nm spectral range (invisible case) differing dramatically from the rich cases, which has characteristic radiation from CH* (390 nm, 431 nm), C$_2^*$ (473 nm, 516 nm, 563 nm). We notice that the emission in the green region (C$_2^*$) have been reported in other setups [8,26] as well. Even non-visible combustions like the $\Phi_j = 0.4$ flame emits radiations at around 310 nm (OH* radical), although the corresponding peak are weaker as compared to the other cases, which is well in
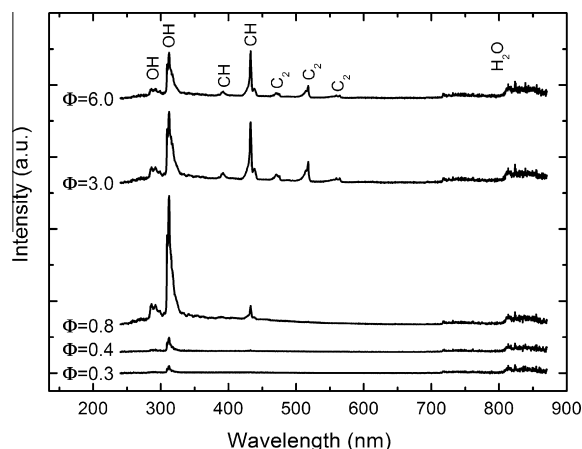
Fig. 2. Emission spectra recorded from flames of U_{JET} = 60 m/s with different equivalent ratios.

line with previous observations [10]. Oxidation reactions proceed in that case too but the light emission suggest different chemical path compared to traditional flames, i.e. with much lower (or vanishing) intermediate CH^* concentration. It can be expected that the chemical oxidation route is strongly affected by the flow and could differ from a traditional reaction diffusion balance.

4.2. Snapshots of the field variables

Figure 3 presents randomly chosen images of the reacting jets showing simultaneous OH/CH_2O PLIF for the turbulent cases. Figure 4 shows separately acquired temperature fields. In Fig. 4 only lean cases are presented, because the assumption of constant Rayleigh cross-section is not valid when the equivalence ratio is 6. One also notes that the inhomogeneous field in the right and bottom corner is a consequence of imperfect shielding of the scatter light and should not be used. At first glance all three cases are similar with a non-reacting jet core surrounded by a layer of formaldehyde and a second layer of OH. These layers coarsely correspond to different temperature levels with a relatively smooth transition from the cold to the hot gases as seen on the temperature snapshots. The thickening effect of relatively small scale turbulence upon the reaction front results in these relatively smooth gradients. These gradients may extend over $\sim 1/3 d–d$ (depending on the location) hence are large enough for being penetrated by coherent structures (e.g. braids) which potentially can distribute the reaction zone. We also note that the levels of the formaldehyde are comparable on all three cases, though with higher value for Φ_j = 0.8. OH levels increase with the jet equivalence ratio, almost doubling from Φ_j = 0.4 to Φ_j = 0.8. The shape of the OH layer also differs significantly from case to case with a continuous barely wrinkled layer in the rich case while the very lean case presents a discontinuous layer with high-OH pockets. This effect is better visualized in Fig. 5 presenting only the fluctuating component of the signals. The case Φ_j = 0.8 lies close to Φ_j = 0.4 with alternating pockets of positive and negative OH–⟨OH⟩. We note that despite of the level differences for the cases Φ_j = 0.8 and Φ_j = 0.4, the fluctuation are comparable indicating a higher fluctuation intensity for the leaner case. In all cases, the OH-signal falls off rapidly at some point towards the axis, hence reaching colder gases. The OH signal also drops below $y/d \sim 3$ indicating a lift-off of the reaction zone as a result of the strong strain at the exit of the nozzle.

The formaldehyde layers appear similar in intensity for all three cases starting with a thin band originating in the shear-layers and surrounding the jet core. Again much less CH_2O is detected for $y/$
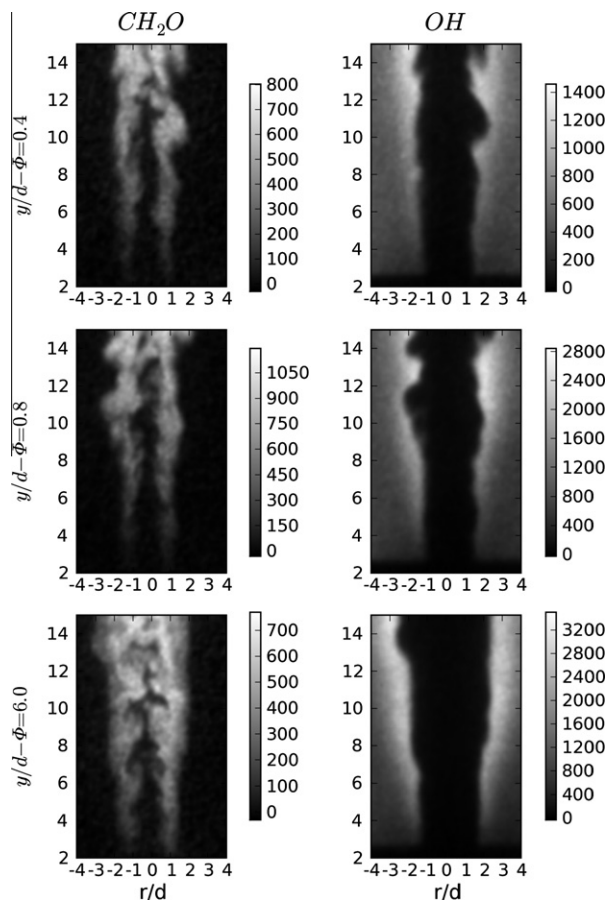

Fig. 3. Simultaneous single shot PLIF images of OH/CH_2O from the flames of U_{JET} = 60 m/s at different equivalent ratios.

$d < 2$ for the richer case while the two lean cases exhibit a longer lift-off, around $y/d \sim 3$. Further downstream, the formaldehyde layers thicken and increase in intensity. It is wrinkled on both sides of the band. The two branches merge downstream of the jet core tip. The increase in intensity seems faster for the richer case. Well in line with the finding above, the CH_2O-brushes are thicker than the large coherent structures so that all cases are well in the distributed reaction regime. Alternating large and small pockets of CH_2O are seen along lines $r/d \sim 1$ for all three cases. The inner limit of the CH_2O brush reveals typical structures seen in a turbulent jet. The outer limit is less wrinkled and mirrors the OH-field limit. To evidence the synchronization of the two species, Fig. 5 superposes the fluctuating OH with iso-levels of fluctuating CH_2O. The positive fluctuations of OH correspond to negative fluctuation of CH_2O (dashed-lines). For the rich case, the fluctuation pattern is relatively simple with long bands. For the two lean cases, alternating pockets of positive and negative values are seen. It corresponds of large pockets of CH_2O would pair with a relatively weak OH-peak/thin OH band. It results from the interaction of chemical reactions with coherent structures usually observed in jets (e.g. rings) highlighting the intermittency of the turbulence/chemistry interaction.

4.3. Gradient of the temperature field

Complementing the observations made in Fig. 4, we focus on the norm of the temperature gradient. The present 2D images do not allow computing the exact gradient but its projection onto the measuring plane. A possible flaw could be that the projection
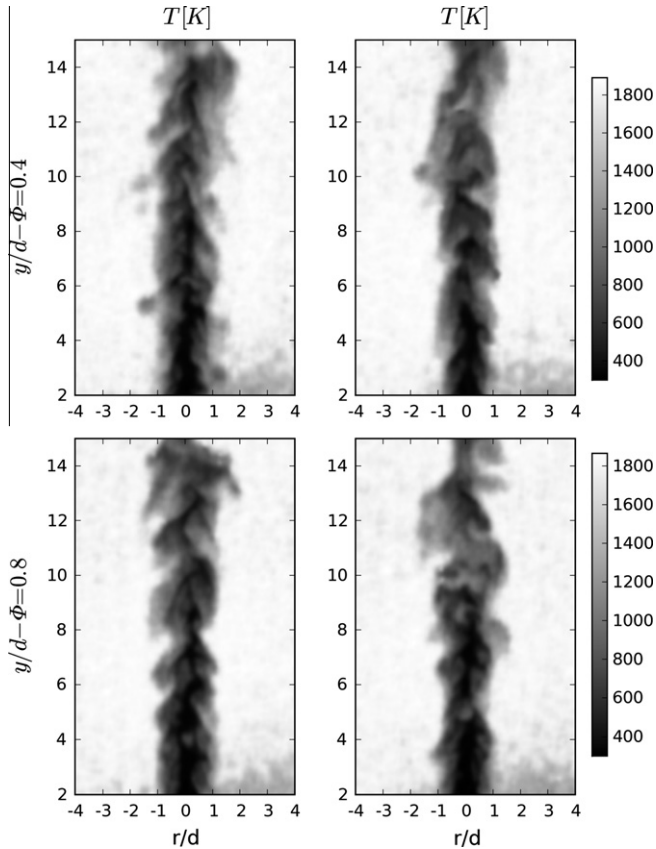
Fig. 4. Typical single shot images of temperature fields for flames with U_{JET} = 60 m/s at different equivalence ratios.

Fig. 5. Fluctuations OH–⟨OH⟩ (fields) and CH_2O–⟨CH_2O⟩ (iso-levels) from the flames of U_{JET} = 60 m/s at different equivalent ratios. Dashed iso-level for negative values and continuous iso-level for positive values.

thickens the front, hence reduces artificially the norm of the gradient. To limit the influence of the projection, we consider solely the maximum along a line, as expressed in Eq. (3). Work reported by Dunn et al. [27] suggests that the maximum of the 3D gradient and of the 2D projected gradient are similar in norm giving credit to the present approach. Figure 6 presents the norm of the gradient for two equivalence ratios in the case high jet speed. The regions of high gradient are concentrated within long thin bands that are nearly parallel to the axis in the proximal region of the jet and are oriented more randomly further downstream with chevron like shape. The value of the norm is similar for both equivalence ratios, although the case Φ = 0.8 seems to exhibit slightly sharper gradients as also shown in Fig. 7. The maximum norm values extracted from the 2D images exceed the values obtained from the laminar flame computations (Table 2). It can be concluded that the thermal thickness of the present reacting jets are determined from the geometry of the burner rather than thermo-diffusive balance. In other words, the thermal thickness scales with the jet shear-layer thickness. The latest scales with the jet diameter so operating with very small jet (millimetre size jet) generates thermal fronts thinner than a corresponding laminar flame. It explains the weak sensitivity of the gradient field to major changes in the stoichiometry. Moreover, Fig. 6 is well in line with the data presented in [27], both for the shape of the high gradient regions and for the maximum intensity.

The distribution of the maximum G of the normalized gradient is presented in Fig. 7. Since the norm of the gradients are similar for Φ = 0.4 and 0.8, normalizing by the laminar flame values introduces a difference of a factor 3. Four flames are considered with two jet velocities per equivalence ratio. Firstly, all distributions have a Gaussian shape, being seemingly symmetric. For the low
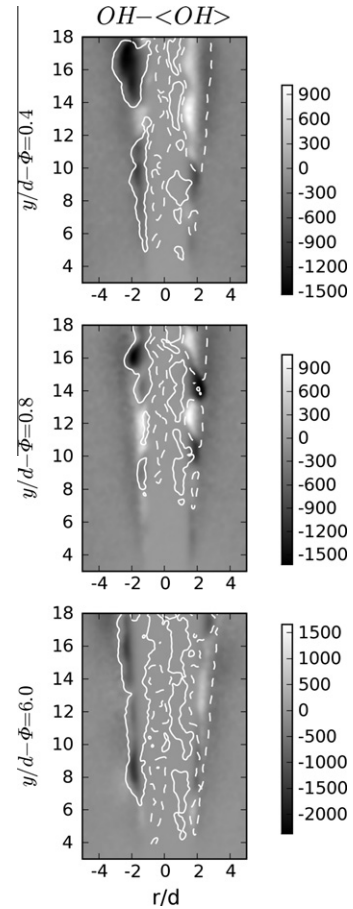
velocity cases, the effect of the flow field (strain rate) is shown to affect the thermal layer that is comparable in thickness with the high speed case. Further, the increase in jet velocity broadens the distributions as result of an increased intensity fluctuation, as will be discussed in the next section. Though, it does not change significantly the median of the G-distribution. From Fig. 7, the temperature gradients are smoother for Φ = 0.8 compared to the counter-flow flames, hence the temperature gradient is disturbed and thickened by the flow. One can estimate that the temperature front thickness δ is inversely proportional to the maximum gradient so that $\delta \sim \delta_T/G$ where δ_T relates to the counter-flow flame (Table 2). From Fig. 7, taking the most probable value of G, one gets $\delta \sim 0.001$ m for all for cases. The front thickness is of the order of the nozzle diameter d explaining why it is relatively insensitive to an increase of the jet velocity. Actually, the larger coherent structures are of the size $\sim d/2$, hence not large enough to further thicken the front. However, these structures as well as the jet shear-layer affect the reactions occurring within the front and disturb the reaction–diffusion balance. The front thickness may therefore change was turbulence affects the shear-layer and the reactions proceed.

4.4. Statistical quantities of the field variables

Figure 8 presents the OH and CH_2O signal distribution at two axial locations, one relatively close to the jet nozzle and the other one downstream of the jet core tip. Both averaged and Root-Mean-Square (rms) values are based on the statistics of 500 single shots.
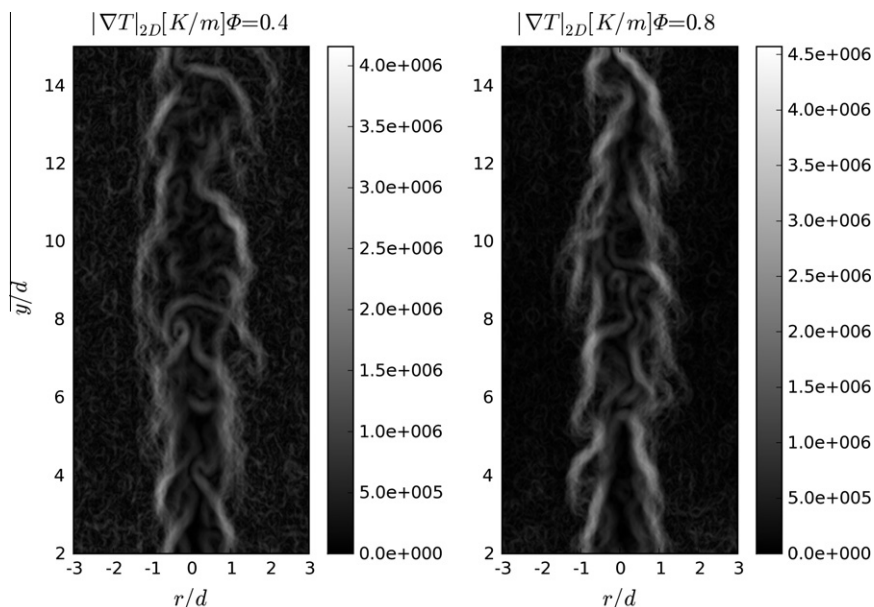
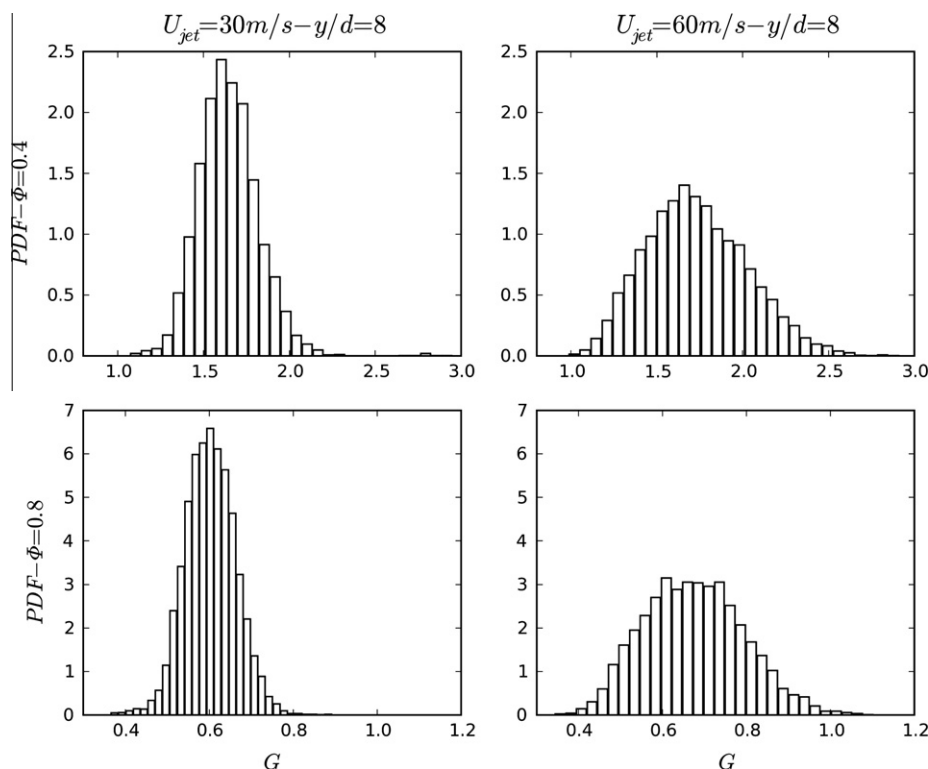**Fig. 6.** Snapshot of the norm of the 2D temperature gradient for the high velocity case.

Fig. 7. Distribution of the normalized gradient norm G as function of Φ and jet velocity at $y/d = 8$.

Concerning that the rms levels are due to flow fluctuations and marginally to noise, each single shot image was smoothed by a low pass filter (Gaussian filter of width 4 SR) before computing the mean and rms, which denotes the final results while keep the flow fluctuations. At $y/d = 4$, both the very lean and rich jet case present similar shapes with higher signal in the rich jet case. In both cases, the CH$_2$O shows peaks centred at $r/d = 0.5$ while the OH peaks extend further from the axis. At this location, the jet core is still present and OH and CH$_2$O exist in the jet shear-layer, this first in the higher temperature region and the second closer to the jet core or lower temperature region. The influence of the turbulent mixing upon the fuel oxidation is evidenced with and increase level of both OH and CH$_2$O with the jet velocity. It advocates that turbulence enhances the mixing of the fresh and vitiated gases, hence prepares efficiently an ignitable mixture where reactions proceed. In addition the relatively high rms levels
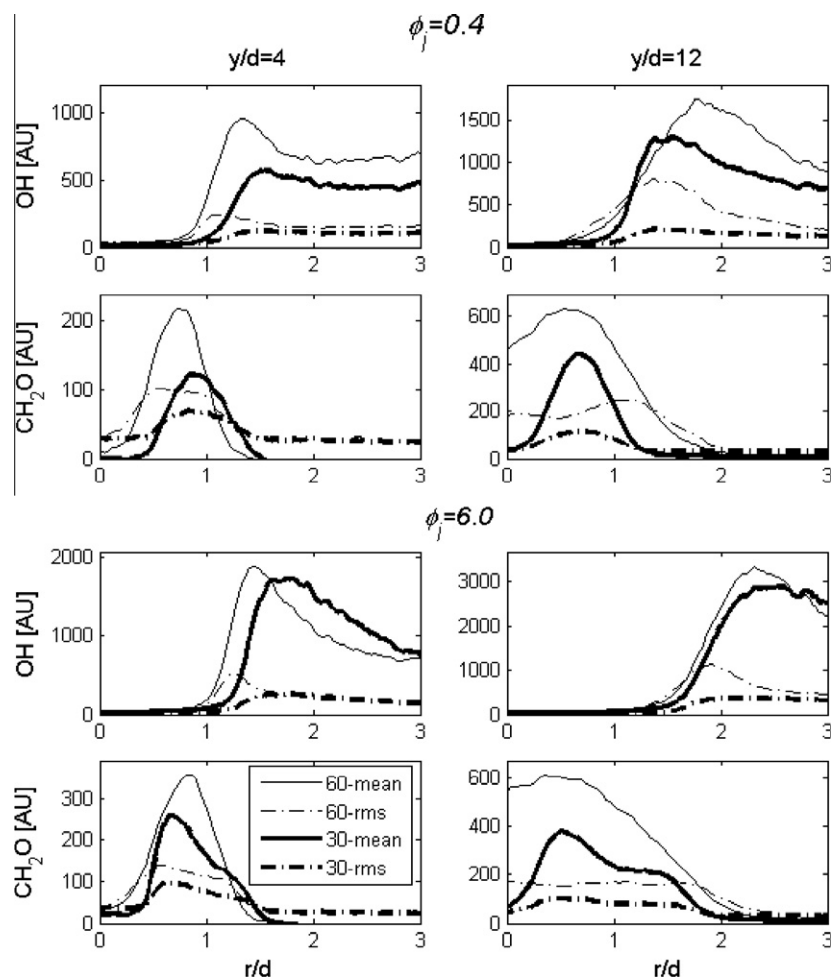
Fig. 8. Mean and Root-Mean-Square (rms) of the OH and CH_2O PLIF signals in arbitrary units along two radial lines for U_{JET} = 30 and 60 m/s.

for CH_2O (up to 50%) and low OH levels would suggest the intermittent passage of pockets of higher formaldehyde concentration similar to the pre-ignition pools reported by Gordon et al. [14].

Further downstream at y/d = 12, the profiles look different depending on the speed. In the laminar case, the reaction layers still extend in the shear-layers, have the same global shape than at y/d = 4 but with higher values and broader peaks. In the turbulent case, the location exceeds the jet core length and a large CH_2O zone can be seen centred at the axis. The OH profiles still present peaks that are centred at $r/d \sim 1.8$ (lean case) and $r/d \sim 2.5$ (rich case). The peaks are broadened compared to the previous location as an effect of the large scale turbulent structures seen previously. For the rich case, the influence of the jet speed can be seen on the formaldehyde plot only as the peak OH is further away from the jet and hence not affected significantly by turbulence. For the very lean case, the peaks of OH and CH_2O overlap and the rms maxima lie in the same location (r/d = 1.2) characterizing the intermittent passages of OH and CH_2O pockets as seen in the snapshots. It indicates a specific interplay between the turbulence and chemical reactions (intermediates concentrations) as seen in the snapshots and will be characterized later in the paper.

Figure 9 presents the effect of the jet equivalence ratio in the turbulence case. Increasing the jet equivalence ratio leads to an increase of both OH and CH_2O signal. At y/d = 4, the peak locations is almost identical regardless of the case and they only differ by amplitude. In addition there is a short overlap between the OH and CH_2O peaks. At y/d = 12, the two lean cases present the same

peak with different amplitudes while the rich jet case presents the OH reaction zone further away from the axis. We note that in the rich jet case, there is a lack of oxygen for complete oxidation; hence partial burnt mixtures can react further with the coflow at radius r/d > 3, while both lean cases lead to fully oxidized mixtures. We note that for all cases the CH_2O peaks are located at $r/d \sim 0.7$ where fresh parcel are mixing with vitiated gases. Increasing the methane content in the central jet improves the formation of CH_2O, leading to stronger peaks at y/d = 4. This point is still valid further downstream for the lean cases but the rich case shows a significant drop in maximum peak value. The OH profile indicated that the reaction zone moves outward for y/d = 12 for the rich case, likely in a region of higher temperatures. This increase of temperature could explain the decrease in CH_2O for the richer case for the region r/d > 1.5.

Figure 10 characterizes the turbulence effect on the reacting layer by plotting the normalized cross-correlation C of OH and CH_2O. As expected from the snapshot in Fig. 3, the C profile exhibit a negative value in the reacting region. Statistically an increase of OH correlates with a decrease of CH_2O. The C-valley moves outwards and broadens as one travels downstream. It follows the increase of the reacting brush thickness. The two lean cases show very similar profiles indicating that the turbulence/chemistry interaction does not depart between the two cases, although significant differences were shown in Fig. 1. The richer case departs from the two others with a C-valley centred further away from the axis. The shape of the valley also evolves differently. While it
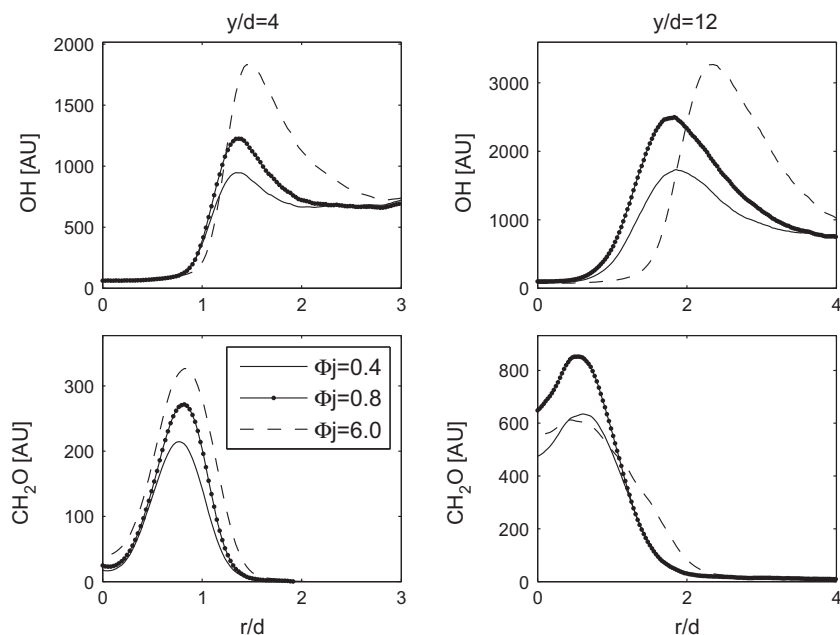
Fig. 9. Mean OH and CH$_2$O PLIF signals along two radial lines for different jet equivalence ratios for U_{JET} = 60 m/s.
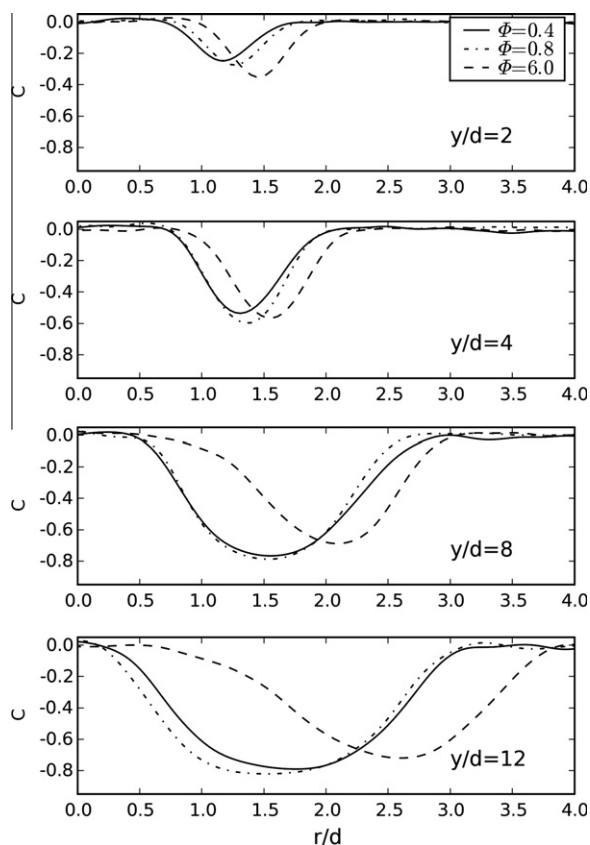

Fig. 10. Normalize cross-correlation C for different jet equivalence ratios along radial lines for U_{JET} = 60 m/s.

stays relatively close to symmetric in the lean cases, the rich case presents an un-symmetric valley from y/d = 8 and downstream. It features a slow decrease with a sharper increase. The different location of the reacting layer in the rich case causes the interactions with different coherent structures with an impact on the combustion properties.

4.5. Distributions scalar and local thicknesses

Figure 11 presents the probability density function of the OH signal at y/d = 12 and radius corresponding to the maxima of rms and the minima of C. In all cases the distributions are wide and relatively flat with seemingly two peaks, one around the mean value and one at zero signals. The latter depicts the passage of relatively cold CH$_2$O containing pockets. The very lean case presents the wider and flatter distribution indicating that even if pockets of strong OH-signal are seen, they are relatively rare (on a statistical base). It follows that the corresponding mean levels are weaker than in the other cases but the fluctuation intensity is comparable. Following the precedent findings, we seek a geometrical characteristic of the intermittent passage of high-OH and high-CH$_2$O pockets and estimate the thickness of the OH and CH$_2$O layers in a band y/d = 12 ± 0.16 (each pixel-line giving a sample), normalize with the jet diameter and present it as a joint probability density functions (jpdf) in Fig. 11. It should be stressed here that the layer thickness was obtained using thresholds on the PLIF signals. Although the choice of these thresholds is not unique, it was verified using several images that the resulting thickness gave an acceptable measure of each brush. The measured thickness values are of the order of the jet diameter indicating that the reaction layer has been distributed to be larger than most of the coherent structures present in a turbulent jet.

For the lean cases, the CH$_2$O brush thickness is around 1d while the OH brush thickness varies between 0.8 and 1.8d. It differs for the rich case where the CH$_2$O brush is thicker than the OH brush as a result of different turbulence chemistry interactions discussed earlier. In addition, for this case, there is clear correlation between the peak width (large OH-pocket) and a thin CH$_2$O peak, and inversely. For the two lean cases, the correlation is less clear as the OH brush is more irregular and wrinkled. In addition, the CH$_2$O brush is constrained between the fresh gas along the axis and the OH layer which limits the fluctuation of the CH$_2$O brush thickness. A similar limitation exists for the rich case but as the OH layer is further away from the axis, it leaves more room for the brush to grow, as measured in Fig. 11. Although the leaner cases do not show an equally clear correlation, the domains of probable events are
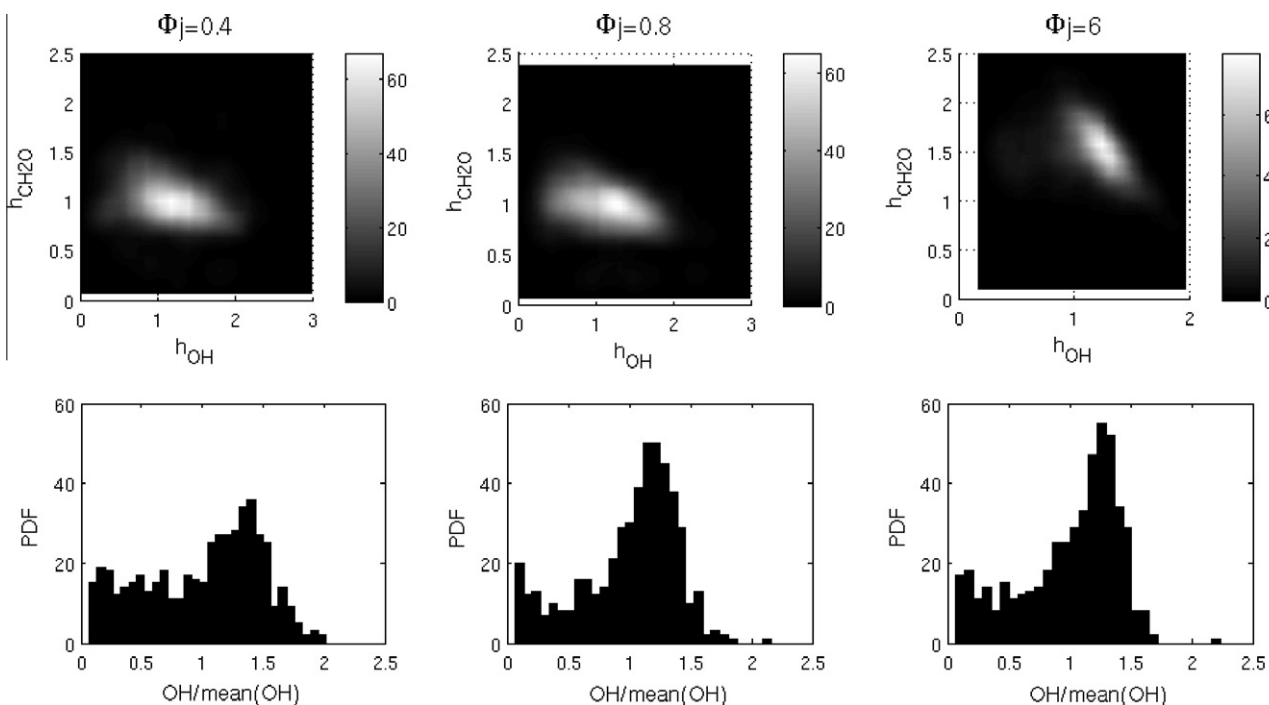
Fig. 11. All turbulent cases data sampled at $y/d = 12$. Top: joint probability density function (PDF) of OH and CH_2O PLIF signal peaks' width (h). Bottom: PDF of the OH signal at the maximums of RMS as seen in Fig. 6.

shaped as a triangle which corners correspond to the two options: thick OH brush/thin CH_2O brush and thin OH brush/thick CH_2O brush excluding having simultaneously thick OH brush/thick CH_2O brush. This was seen on the snapshots presented earlier.

5. Summary and conclusions

High resolution planar laser-induced fluorescence (PLIF) technique was used for the study of turbulence/combustion interaction in a laboratory scale pilot jet burner operating at very high Karlovitz numbers. Both visible and non-visible reaction layers were observed whereas all cases were found to emit radiations indicating the presence of OH. The oxygen depleted case (rich jet) presented the highest emission and OH/CH_2O signal, although the oxidation is distributed in a larger volume compared to the distributed flame ($\Phi_j = 0.8$). The very lean case ($\Phi_j = 0.4$) was emitting the least in accordance with the extreme dilution of the fuel. Further, the structure of the reaction layer was found to consist of two concentric layers, one containing CH_2O surrounded by one containing OH. Both layers are thickened by the turbulent structures (when present) distributing the reaction over thick layers. The thickness of these layers varies with alternating thickening and thinning. The pattern of this phenomena suggested that it is driven by the large coherent structures (rings and helices) present in the jet. If the very lean case presents lower mean levels, evidences were given that suggest a stronger intermittence with broader point distributions. The strong intermittence and the high dilution drive the invisible combustion in that particular case.

The present results suggest a complex and intermittent interplay between turbulence and chemical oxidation involving the coherent structures arising in the jet shear-layer. The result of the interaction consists of thick brushes of OH and CH_2O with alternating thicknesses. Indeed the dynamics of the reaction brushes was found to be dependent on the thermo-chemistry of the jet. Large differences were seen between the two lean cases and the rich case (close to MILD). Despite obvious differences in

term of visibility, the two lean cases present very similar characteristics in term of turbulence/chemistry interaction, although the leaner case presents lower OH levels. It also implies that flameless combustion for gas turbine application (lean flameless) would certainly differ in term of turbulence/chemistry interaction (hence burner design) compared to a flameless furnace (MILD combustion).

Future work should focus on identifying the exact effect, upon combustion, of the different coherent structures present in a turbulent jet. In particular the role of braids could be vital and will be investigated using large eddy simulation.

Acknowledgments

References

[1] R.W. Bilger, S.B. Pope, K.N.C. Bray, J.F. Driscoll, Proc. Combust. Inst. 30 (2005) 21–42.
[2] T. Poinsot, D. Veynante, Theoretical and Numerical Combustion, RT Edwards, Philadelphia, USA, 2001.
[3] J.A. Wunning, J.G. Wunning, Prog. Energy Combust. Sci. 23 (1997) 81–94.
[4] M. Katsuki, T. Hasegawa, Proc. Combust. Inst. 27 (1998) 3135–3146.
[5] A. Cavaliere, M. de Joannon, Prog. Energy Combust. Sci. 30 (2004) 329–366.
[6] F. Weinberg, Combust. Sci. Technol. 121 (1996) 3–22.
[7] R. Weber, A.L. Verlaan, S. Orsino, N. Lallemant, J. Inst. Energy 72 (1999) 77–83.
[8] M. Mortberg, W. Blasiak, A.K. Gupta, Combust. Sci. Technol. 178 (2006) 1345–1372.
[9] G.G. Szego, B.B. Dally, G.J. Nathan, Combust. Flame 156 (2009) 429–438.
[10] C. Duwig, D. Stankovic, L. Fuchs, G. Li, E. Gutmark, Combust. Sci. Technol. 180 (2008) 279–295.
[11] R. Lueckerath, W. Meier, M. Aigner, J. Eng. Gas Turb. Power 130 (2008).
[12] P. Gopalakrishnan, M.K. Bobba, J.M. Seitzman, Proc. Combust. Inst. 31 (2007) 3401–3408.
[13] R. Cabra, T. Myhrvold, J.Y. Chen, R.W. Dibble, A.N. Karpetis, R.S. Barlow, Proc. Combust. Inst. 29 (2003) 1881–1888.

[14] R.L. Gordon, A.R. Masri, E. Mastorakos, Combust. Flame 155 (2008) 181–195.
[15] E. Oldenhof, M.J. Tummers, E.H. van Veen, D.J.E.M. Roekaerts, Combust. Flame 157 (6) (2010) 1167–1178.
[16] I.B. Ozdemir, N. Peters, Exp. Fluids 30 (2001) 683–695.
[17] B.B. Dally, A.N. Karpetis, R.S. Barlow, Proc. Combust. Inst. 29 (2003) 1147–1154.
[18] P.R. Medwell, P.A.M. Kalt, B.B. Dally, Combust. Flame 152 (2008) 100–113.
[19] Cantera, Object-Oriented Software for Reacting Flows, 2006. <http://www.cantera>.
[20] G.P. Smith, D.M. Golden, M. Frenklach, N.W. Moriarty, B. Eiteneer, M. Goldenberg, C.T. Bowman, R.K. Hanson, S. Song, W.C. Gardiner Jr., V.V. Lissianski, Z. Qin, GRI3.0. <http://www.me.berkeley.edu/gri_mech/>.

[21] D. Demare, F. Baillot, Phys. Fluids 13 (2001) 2662–2670.
[22] M.J. Dunn, A.R. Masri, R.W. Bilger, Combust. Flame 151 (2007) 46–60.
[23] J.A. Sutton, J.F. Driscoll, Opt. Lett. 29 (2004) 2620–2622.
[24] L. Rudin, S. Osher, E. Fatemi, Physica D 60 (1992) 259–268.
[25] R.W. Schefer, W.D. Kulatilaka, B.D. Patterson, T.B. Settersten, Combust. Flame 156 (2009) 1234–1241.
[26] T. Hasegawa, S. Mochida, A.K. Gupta, J. Propul. Power 18 (2002) 233–239.
[27] M.J. Dunn, A.R. Masri, R.W. Bilger, Robert S. Barlow, Flow Turb. Combust. 85 (2010) 621–648.